Hindawi
Journal of Chemistry
Volume 2022, Article ID 3528170, 18 pages
https://doi.org/10.1155/2022/3528170

Research Article

Theoretical Study of the Structural, Optoelectronic, and Reactivity Properties of N-[5′-Methyl-3′-Isoxasolyl]-N-[(E)-1-(-2-)] Methylidene] Amine and Some of Its Fe^{2+}, Co^{2+}, Ni^{2+}, Cu^{2+}, and Zn^{2+} Complexes for OLED and OFET Applications

Hilaire Tendongmo,[1] **Stanley Numbonui Tasheh**,[1] **Didier Aymard Fouegue Tamafo**,[2] **Fritzgerald Kogge Bine**,[1] **and Julius Numbonui Ghogomu**[1,3]

[1]*Research Unit of Noxious Chemistry and Environmental Engineering, Department of Chemistry, Faculty of Science, University of Dschang, P.O. Box 67, Dschang, Cameroon*
[2]*Department of Chemistry, Higher Teacher Training College Bertoua, University of Bertoua, P.O. Box 652, Bertoua, Cameroon*
[3]*Department of Chemistry, Faculty of Science, The University of Bamenda, P.O. Box 39, Bambili, Bamenda, Cameroon*

Correspondence should be addressed to Julius Numbonui Ghogomu; ghogsjuju@hotmail.com

Received 3 April 2022; Accepted 29 June 2022; Published 22 July 2022

Academic Editor: Josefina Pons

Herein, we report the structural, electronic, and charge transfer properties of N-[5′-methyl-3′-isoxasolyl]-N-[(E)-1-(-2-thiophene)] methylidene] amine (L) and its Fe^{2+}, Co^{2+}, Ni^{2+}, Cu^{2+}, and Zn^{2+} complexes (dubbed A, B, C, D, and E, respectively) using the density functional theory (DFT). All molecules investigated were optimized at the BP86/def2-TZVP/RI level of theory. Single point energy calculations were carried out at the M06-D3ZERO/def2-TZVP/RIJCOSX level of theory. Reorganization energies of the hole and electron (λ_h and λ_e) and the charge transfer mobilities of the electron and hole (μ_e and μ_h) have been computed and reported. The λ_e and λ_h values vary in the order D > E > A > B > C > L and E > A > D > L > C > B, respectively, while μ_e and μ_h vary in the order B > C > L > A > E > D and C > B > A > L > E > D, respectively. μ_h of B (39.5401 $cm^2 \cdot V^{-1}S^{-1}$) and C (366.4740 $cm^2 \cdot V^{-1}s^{-1}$) is remarkably large, suggesting their application in organic light-emitting diode (OLED) and organic field-effect transistor (OFET) technologies. Electron excitation analysis based on time-dependent (TD)-DFT calculations revealed that charge transfer excitations may significantly affect charge transfer mobilities. Based on charge transfer mobility results, B and C are outstanding and are promising molecules for the manufacture of electron and hole-transport precursor materials for the construction of OLED and OFET devices as compared to L. The results also show that L and all its complexes interestingly have higher third-order NLO activity than those of para-nitroaniline, a prototypical NLO molecule.

1. Introduction

The rapid development of optoelectronic technologies based on organic molecules has been propelled by the growing desire for eco-friendly, light, but flexible electronic devices [1–3]. The expansion of industries associated with the production of flexible, low-cost electronic devices such as organic field-effect transistors (OFETs), organic solar cells (OSCs), and organic light-emitting diodes (OLEDs) is on the rise [4, 5]. OLEDs and OFETs have emerged as potential display, lighting, low-cost, flexible, lightweight, and wearable electronic device technologies [6, 7]. Due to the existence of heterocyclic rings and their pi-conjugated frameworks, isoxazole-thiophene Schiff bases are interesting possibilities in optoelectronics [8]. The highest occupied molecular orbital (HOMO) and the lowest unoccupied molecular orbital (LUMO) energy levels, as well as adequate electron and hole mobilities, determine the optoelectronic properties of such devices [9, 10].

Charge transfer mobilities in such compounds are governed by their conjugated frameworks and intermolecular orbital overlap [9]. Although there are numerous

suggestions for building small molecules with desirable optoelectronic properties, there is a paucity of information on charge carrier mobilities in organic materials [11, 12]. Furthermore, carrier mobility is a critical property of every semiconducting material, determining its appropriateness for a wide range of electronic device applications. The magnitude of this parameter depends on molecular characteristics and molecular packing modes, and it serves as a reference for optimizing field-effect mobility in organic electrical devices [13]. Working conditions, such as measurement methods, microstructural characteristics of dielectric layers, and semiconductor film deposition, frequently influence experimental studies on charge transfer mobilities [13]. The use of theoretical simulation methods to determine charge transfer mobility and related properties is an important and cost-effective option [14, 15]. In this light, and despite their importance, isoxazole-thiophene-based compounds have received less theoretical and experimental attention, demanding more research in this area. Given the fact that coordination with metal is most likely to increase the thermal stability and mechanical properties of these molecules, additional research into this area is critical. This work aims at studying theoretically the structural, optoelectronic, and reactivity properties of N-[5′-methyl-3′-isoxasolyl]-N-[(E)-1-(-2-thiophene)] methylidene] amine (L) (see Figure 1). The investigation of some of its complexes, $[Fe(L)_2(H_2O)_2]^{2+}$ denoted as A, $[Co(L)_2(H_2O)_2]^{2+}$denoted as B, $[Ni(L)_2(H_2O)_2]^{2+}$ denoted as C, $[Cu(L)_2(H_2O)_2]^{2+}$ denoted as D, and $[Zn(L)_2(H_2O)_2]^{2+}$ denoted as E with transition metal ions for OLED and OFET applications, was also carried out. Accordingly, the nonlinear optical (NLO) properties of the ligand (L) and its complexes have also been investigated as a result of its π-conjugated framework, which may confer NLO activity.

2. Computational Details

The geometries of the ligand and the metal complexes were fully optimized with ORCA 4.1.0 programme package [16] using the density functional theory (DFT). The DFT was employed in this study as it is appropriate for the study of coordination compounds [17]. All input files for geometry optimization were prepared with the Avogadro 1.2.1 visualization tool [18] in conjunction with the BP86 functional [19] alongside the def2-TZVP Ahlrichs basis set [20]. The BP86 functional is very good for geometry optimization and vibrational frequency calculations [21]. The resolution-of-the-identity (RIJ) approximation [22] was used to speed up calculations with minimal loss in accuracy. Moreover, Grimme's atom-pairwise dispersion (the Becke–Johnson damping scheme, D3BJ) [23] was used to account for long-range dispersion interactions since the pure exchange-correlation functionals fail to properly account for such interactions.

To ascertain that the most stable geometries of the investigated molecules were local minima on their potential energy surfaces, vibrational harmonic frequencies were calculated at the same level of theory as that used for geometry optimizations. No imaginary frequencies were obtained. Single point energy (SPE) calculations were then performed on the BP86-optimized geometries of neutral, cationic, and anionic species of the studied molecules using the Minnesota functional, M06 [24]. The combined RIJ and chain of sphere approximations were employed as RIJCOSX [25, 26] to speed up calculations with minimal loss in accuracy. The SP energy results were further used to calculate the ionization potentials (IPs), electron affinities (EAs), and the global reactivity descriptors including the hardness (η), softness (S), electronegativity (χ), chemical potential (μ), and electrophilicity (ω). The adiabatic IP and EA are calculated using equations (1) and (2), respectively, while the global reactivity descriptors are calculated using equations (3)–(6):

$$\mathrm{IP} = E_{(N-1)} - E_N, \tag{1}$$

$$\mathrm{EA} = E_{(N)} - E_{(N+1)}, \tag{2}$$

$$\eta = \frac{(\mathrm{IP} - \mathrm{EA})}{2}, \tag{3}$$

$$\chi = \frac{(\mathrm{IP} + \mathrm{EA})}{2}, \tag{4}$$

$$\mu = -\chi, \tag{5}$$

$$\omega = \frac{\mu^2}{2\eta}, \tag{6}$$

where $E_{(N-1)}$, E_N, and $E_{(N+1)}$ are the energies of the cationic, neutral, and anionic forms of the investigated molecules. Also, local reactivity descriptors (LRDs), as well as molecular electrostatic potential (MEP) maps, were used to locate reactive sites in the studied molecules. A common descriptor here is the Fukui function, which measures the change in the chemical potential of a system as a result of a change in the number of electrons in the molecule and hence determines the reactivity of individual atoms in a molecule [27]. According to Yang and Mortier [28], the Fukui function at an atom k can be approximated as

$$f_k^+ = q_k(N) - q_k(N+1), \tag{7}$$

$$f_k^- = q_k(N-1) - q_k(N), \tag{8}$$

$$f_k^0 = \frac{1}{2}\left[q_k(N+1) - q_k(N-1)\right], \tag{9}$$

where $q_k(N)$, $q_k(N+1)$, and $q_k(N-1)$ are charges of the neutral, anionic, and cationic species of k. f_k^+, f_k^-, and f_k^0 describe the electrophilic, nucleophilic, and free radical behaviours of the individual atoms, respectively. Moreover, another powerful LRD is the dual descriptor Δf_k, which simultaneously defines the nucleophilic and electrophilic sites within a molecule. Δf_k can therefore be calculated from the Fukui functions [29, 30] using the following equation:

$$\Delta f_k = f_k^+ - f_k^-. \tag{10}$$

Generally, high values of Δf_k (i.e., $\Delta f_k > 0$) indicate atom k's susceptibility to a nucleophilic attack (acts as an

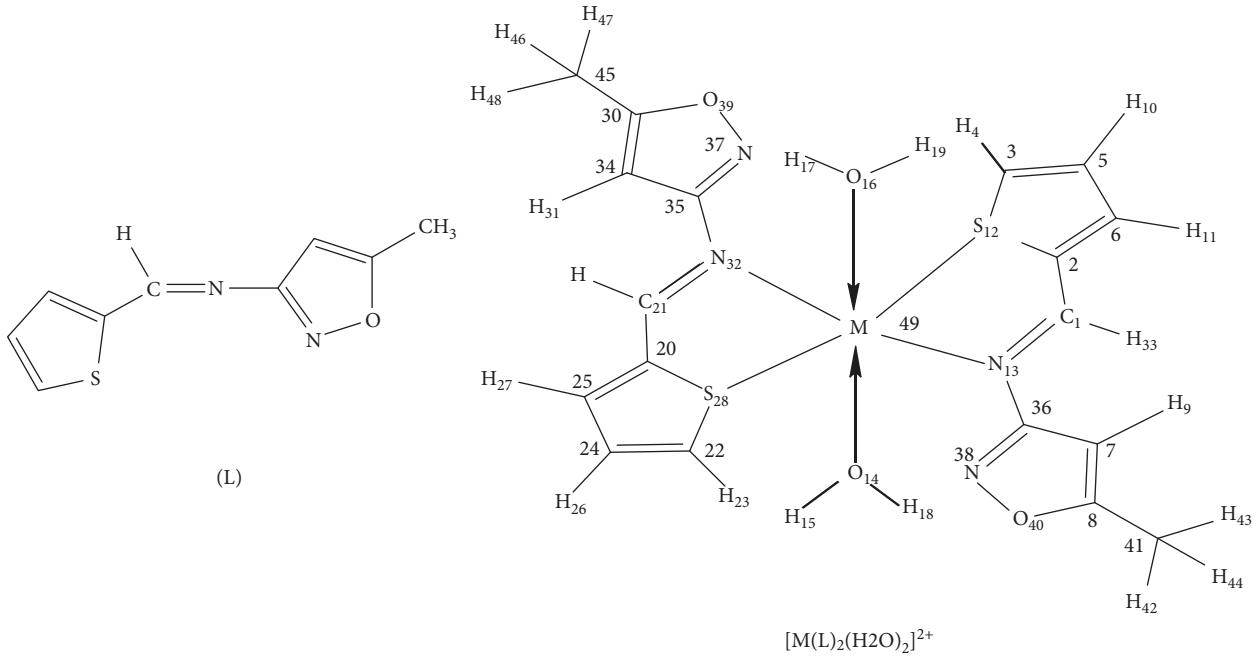

Figure 1: Structure of ligand (L) and metal complexes where M = Fe^{2+}, Co^{2+}, Ni^{2+}, Cu^{2+}, and Zn^{2+}.

electrophile), while on the contrary, low values of Δf_k ($\Delta f_k > 0$) suggest that atom k is prone to an electrophilic attack and, in this case, acts as a nucleophile [29, 30].

Bader's method, quantum theory of atoms in molecules (QTAIM) alongside the electron localization function (ELF), and the localized orbital locator (LOL) topological descriptors via the Multiwfn 3.7 software package [31] were used to characterize bonding interactions in the studied compounds. The electron and hole distributions in the studied molecules were investigated using the TD-DFT method. Charge transfer properties, reorganization energies, charge transfer integrals, charge transfer rates, and charge transfer mobilities were calculated by making use of the Marcus theory. This theory describes charge transfer as a self-exchange electron transfer reaction between a neutral molecule and a neighbouring anionic or cationic species [31–33]. The charge transfer rate K_{CT} can be modelled by the classical Marcus theory as

$$K_{CT} = \left(\frac{4\pi^3}{h^2 \lambda K_b T}\right)^{(1/2)} V_{i,j}^2 \exp\left[-\frac{\lambda}{4K_b T}\right], \tag{11}$$

where $V_{i,j}$ is the transfer integral between two adjacent species i and j, λ is the reorganization energy, K_B is the Boltzmann constant, T is the absolute temperature, and h is Planck's constant. From Marcus' equation, the reorganization energy (λ) reflects the changes in the geometry of the molecules when going from the neutral to the ionized state and vice versa [34], while $V_{i,j}$ is concerned with the strength of the interaction between the species i and j and measures the ability of charge carriers to move across the species i and j [35, 36]. Generally, high charge carrier mobilities are enhanced by low reorganization energies and high charge transfer integrals [37]. Both internal and external contributions are often encountered in the calculation of reorganization energy. The former contribution deals with geometric changes when electron transfer takes place, while the latter contribution comes from changes in the surrounding media accompanying the charge transfer and is negligible [38]. Thus, the internal reorganization energy of holes and electrons can be calculated using equations (12) and (13) the following equations, respectively:

$$\lambda_h = \left(E_0^+ - E_+^+\right) + \left(E_+^0 - E_0^0\right), \tag{12}$$

$$\lambda_e = \left(E_0^- - E_-^-\right) + \left(E_-^0 - E_0^0\right), \tag{13}$$

where E_0^0, E_+^+, and E_-^- are energies of the neutral, cationic, and anionic forms of the molecule computed on the optimized geometries of the neutral, cationic, and anionic structures of the molecules, respectively. E_0^+ and E_0^- are the energies of cationic and anionic species computed on the optimized geometry of the neutral species, respectively, while E_+^0 and E_-^0 are the energies of neutral species, computed on the optimized geometries of cationic and anionic species, respectively.

The charge transfer integrals [38] of holes and electrons can be estimated from Koopman's theorem as half the splitting energy of the two highest occupied molecular orbitals (HOMOs), ε_H and ε_{H-1}, and the two lowest unoccupied molecular orbitals (LUMOs), ε_{L+1} and ε_L, respectively of the molecular dimers based on the molecules and calculated according to the following equations:

$$V_e = \frac{1}{2}\left(\varepsilon_{L+1} - \varepsilon_L\right), \tag{14}$$

$$V_h = \frac{1}{2}\left(\varepsilon_H - \varepsilon_{H-1}\right), \tag{15}$$

where ε_H and ε_{H-1} denote the energy levels of the HOMO and HOMO – 1 and ε_{L+1} and ε_L denote the energy levels of

the LUMO + 1 and LUMO, respectively. The KT method was used in this study for its efficiency with symmetric molecules. It should be noted that the studied molecules were not perfectly symmetric. $V_{i,j}$ was calculated by the use of SP energies of co-facial dimers separated by an intermolecular distance of 4.0 Å.

Finally, the charge transfer mobility, the governing parameter for charge transfer properties, was calculated using the following equation:

$$\mu = \frac{ed^2 K_{CT}}{2K_B T}, \tag{16}$$

where e is the electric charge in coulombs, K_{CT} is the charge transfer rate in s^{-1}, d is the intermolecular distance between the two monomers in the dimer in cm^2, K_B is the Boltzmann constant in JK^{-1}, and T is the temperature in K.

To highlight the impact of complexation on the NLO properties of the ligand L, the static mean polarizability ($\langle\alpha\rangle$), the total static first hyperpolarizability (β_{tot}), the vector component of the first hyperpolarizability (β_{vec}), and the average second hyperpolarizability (γ) were calculated at the wB97X-D/6-311++G level of theory.

3. Results and Discussion

3.1. Structural and Geometric Analysis. The ground state geometries of L and its metal (II) complexes were optimized in the gas phase using the BP86 alongside the def2-TZVP basis set as earlier mentioned. Each complex consists of a central metal ion, two water molecules, and two ligand molecules each as proposed by Shakru and collaborators [39]. Some gas-phase geometrical parameters of L and its 3d metal complexes studied are presented in Table 1.

The results show that the M-S_i ($i = 12$ and 28) bond lengths are in the range of 2.445 Å for A and 3.038 Å for D. The great discrepancy for D may suggest its loosely bound nature. The results from the table also indicate that the M-O (H_2O) bonds are shorter in D with a bond length value of 2.010 Å followed by C. The longest M-O (H_2O) bond length has been observed for compound A with a value of 2.196 Å, suggesting that one of the water ligands is loosely bound to the central Fe^{2+} ion in the complex. Upon complexation, there is a slight increase in the azomethine bond length (C = N). The significant difference in some values of bond lengths (C_i = N_i, M-S_i, M-N_i, and M-O_i) may be associated with Jahn-Teller distortions [35]. The metal-ligand bond angles indicate distorted geometries around the central metal ions in the complexes studied, which may result from distortions imposed by the chelate rings.

The optimized Cartesian coordinates and optimized geometries of the studied compounds are provided in Tables S1–S6 and Figure S1 of the accompanying electronic supplementary material (ESM), respectively.

3.1.1. Vibrational Analysis. To ascertain the suitability and the validity of our method of computation, vibrational frequencies were calculated and compared to experimental results obtained elsewhere [40, 41]. Relevant theoretical IR vibrational frequencies of the molecules investigated were calculated at the BP86/def2-TZVP level of theory, and the assignment of the vibrational modes was aided by Chemcraft [42], and some important vibrational frequencies are reported in Table 2.

Table 1: Gas-phase optimized geometric parameters of molecules studied at BP86/def2-TZVP level of theory.

Geometric parameter	L	A	B	C	D	E
Bond length (Å)						
M-S_{12}	—	2.619	2.470	2.517	3.027	2.785
M-S_{28}	—	2.445	2.469	2.516	3.038	2.814
M-N_{13}	—	2.128	2.116	2.086	2.024	2.104
M-N_{32}	—	2.185	2.117	2.086	2.024	2.100
M-O_{14}	—	2.196	2.121	2.076	2.010	2.106
M-O_{16}	—	2.056	2.122	2.076	2.010	2.105
S_{12}-C_2	1.740	1.750	1.744	1.760	1.748	1.751
S_{28}-C_{20}	1.740	1.756	1.745	1.760	1.748	1.751
C_1=N_{13}	1.292	1.312	1.318	1.308	1.315	1.312
C_{21}=N_{32}	1.292	1.313	1.318	1.308	1.315	1.312
Bond angles (°)						
O_{14}-M-N_{13}	—	88.7	88.4	85.7	88.0	85.9
O_{14}-M-N_{32}	—	90.9	91.7	94.3	92.0	94.2
O_{16}-M-N_{13}	—	94.5	91.6	94.3	92.0	93.9
O_{16}-M-N_{32}	—	85.7	88.3	85.7	88.1	86.0
O_{14}-M-S_{12}	—	82.9	90.5	89.3	97.3	92.8
O_{14}-M-S_{28}	—	88.0	89.6	90.7	82.4	86.7
O_{16}-M-S_{12}	—	86.1	89.5	90.7	82.9	88.0
O_{16}-M-S_{28}	—	102.9	90.4	89.3	97.4	86.0
Dihedral angles (°)						
$S_{12}MN_{32}C_{21}$	—	−143.6	163.5	−148.2	−156.6	−149.2
$S_{28}MN_{13}C_1$	—	−148.7	−164.2	148.2	157.5	150.2

Table 2: Calculated (scaled) and experimental IR frequencies of ligand (MITMA) and its metal complexes at the BP86/def2-TZVP level of theory.

Assignment	$\overline{\vartheta}$ (C=N)		$\overline{\vartheta}$ (M-N)		$\overline{\vartheta}$ ((M-S)	
	ν^a_{cal}	ν^b_{exp}	ν_{cal}	ν_{exp}	ν_{cal}	ν_{exp}
L	1607	1613	—	—	—	—
$[Fe(L)_2(H_2O)_2]^{2+}$	1549	—	521	—	576	—
$[Co(L)_2(H_2O)_2]^{2+}$	1547	1636	521	460	577	409
$[Ni(L)_2(H_2O)_2]^{2+}$	1569	1633	529	469	572	405
$[Cu(L)_2(H_2O)_2]^{2+}$	1570	1639	520	463	581	408
$[Zn(L)_2(H_2O)_2]^{2+}$	1574	1636	529	450	579	412

ν^a_{cal} and ν^b_{exp} are the calculated (scaled) and experimental IR frequencies of vibration, respectively.

The calculated frequencies were scaled by a factor of 0.9953 [43] in accordance with the BP86/def2-TZVP level of theory. In an attempt to assess the extent of agreement between the scaled calculated IR frequencies and the experimentally observed values, the following correlation equation (17) was established for the ligand and its complexes:

$$\overline{\vartheta}_{scaled} = \overline{\vartheta}_{exp} - 49.34. \tag{17}$$

The correlation coefficient, $R^2 = 0.993$, confirms the suitability of our method of computation.

Table 2 shows significant shifts in IR vibrations that occurred for the C = N, M-N, and M-S bonds, implying that their vibrations are affected by complexation. The C = N bonds are shortened upon complexation. This can be supported by the great discrepancies in the vibrational frequencies of the ligand and complexes.

Vibrations in the region 1570–1610 cm^{-1} are assigned to the stretching vibrations of the azomethine bond (C = N) in the complexes. The shift of the azomethine vibration suggests the coordination of the azomethine nitrogen to the central metal ion. Moreover, the vibrations around 520–530 cm^{-1} are attributed to the stretching vibrations of the M-N bond in the complexes. Also, the vibrations around 570–582 cm^{-1} are likened to the stretching vibrations of the M-S bond in the complexes. In addition, IR spectra of all metal complexes showed vibrations around 3610–3745 cm^{-1} associated with the presence of water molecules in the coordination sphere. The presence of these vibrations is in line with those predicted by Ref. [39], further supporting the validity of our method.

3.1.2. QTAIM Analysis. Bader's theory is remarkable and reliable for the description of intermolecular contacts of atoms in molecules, as it is based on the electron density (ρ (r)) and its Laplacian ($\nabla^2\rho$ (r) > 0) [44, 45]. Moreover, in the realm of QTAIM, the determination of the strength and character of a chemical interaction is based on the properties of the bond at the BCP [46–48].

In this study, some topological parameters at the BCP were used to characterize the nature of interactions in the investigated chemical species. Generally, values of ρ (r) > 0.2 a.u., $\nabla^2\rho$ (r) < 0, and $-G(r)/V(r) < 1$ are indicative of covalent bonding interactions, where $G(r)$ is the kinetic energy density and $V(r)$ is the potential energy density at the BCP. Likewise, ρ (r) < 0.1 a.u., $\nabla^2\rho$ (r) > 0, and $-G(r)/V(r) > 1$ are characteristics of noncovalent interactions. Moreover, when ρ (r) < 0.1 a.u., $\nabla^2\rho$ (r) > 0, and $0.5 < -G(r)/V(r) < 1$, the interactions are considered as partially or partly covalent [49]. Besides another parameter, namely, total energy density, H (r) was also used to characterize the nature of interactions in this work. The values of H (r) and its sign determine whether the accumulation of charge at a given point r is stabilizing (H (r) < 0); else, destabilizing (H (r) > 0) [50]. H (r) tends to be negative for interactions involving sharing of electrons (covalent) and positive for ionic interactions. However, for metal-ligand (M-L) interactions, H (r) is negative and closer to zero, while $\nabla^2\rho(r) > 0$ [51, 52]. Pertinent topological parameters at the BCPs of the M-L bond as well as hydrogen bonds (HB) are reported in Table 3 and the molecular graphs are presented in Figure S2.

H-bonds, if present, may be classified as conventional or classical (characterized and $\nabla^2\rho$ (r) > 0.044 a.u.) or "nonconventional (characterized by $\nabla^2\rho$ (r) < 0.024 a.u.). Conventional H-bonds are those in which the hydrogen atom is between two electronegative atoms: one acting as the donor and the other as the acceptor atom. Those H-bonds different from the above mentioned are said to be nonconventional [53].

Figure S2 shows the presence of hydrogen bonding (HB), between the N atom of the isoxazole moiety and water molecules (N-HO) in all the complexes except B. The HBs were classified according to Trendafilova [47] based on the electron density and its Laplacian at the BCP. It is clear from Table 3 that all the HBs in the complexes may be considered conventional as ρ ((r)) > 0.015 a.u. and $\nabla^2\rho(r) > 0.044$ a.u. Moreover, in an attempt to estimate the strength of the HB, its energy equation as proposed by Espinosa et al. [54] was used:

$$E_{\text{int}} = \frac{1}{2}V(r), \tag{18}$$

where E_{int} is the interatomic interaction energy as reported in Table 3 and $V(r)$ potential energy density. Careful inspection of Table 3 shows that all the HBs interatomic interaction energies of the complexes studied are in the range of 12–17 kcal/mol. Hence, HB strength is medium in C and E and stronger in D and A in line with Jeffrey's classification [55] whereby the strength of an HB may be characterized as weak, medium, or strong based on its interaction energy, 0–4 kcal/mol, 4–14 kcal/mol, and 14–40 kcal/mol, respectively.

3.1.3. Electron Localization Function and Localized Orbital Locator. To further characterize the bonding interactions in the complexes studied, electron localization function (ELF), η (r), as well as the localized orbital locator (LOL), ν (r), was used. The values of η (r) and ν (r) obtained were aided by the topological analysis at BCPs and are reported in Table 3. In general, the ELF and LOL values are in the range of 0.0 to 1.0 as they convey similar information and interpretation with LOL having a more decisive meaning [56]. Moreover, large values of ELF and LOL (>0.5) are dominated by regions with high electron localization (covalent). By inspection, Table 3 shows that all bonding interactions considered here have η (r) and ν (r) values less than 0.5, further supporting the noncovalent nature of metal-ligand bonding interactions as predicted by QTAIM.

3.2. Reactivity Descriptors

3.2.1. Frontier Molecular Orbitals (FMOs). Here, an analysis of the FMO was carried out to gain insight into the distribution of electrons in the molecular entities. The HOMO orbitals can donate electrons, whereas the LUMOs are regarded as acceptors of electrons. The energy gap between the HOMO and LUMO is likened to hardness, which is related to stability and may well be vital for describing intermolecular charge transfer in complexes [57]. Most often, chemical species with high HOMO-LUMO energy gap values are said to be stable and may tend to resist any chemical changes; else, they tend to be reactive and easily polarizable [58]. The energies of the HOMO and LUMO and energy gap were obtained from the single point energy (SPE) calculations using the M06/def2-TZVP/D3ZERO level of theory of the optimized geometry at the BP86/def2-TZVP/

Table 3: Computed values of ρ (r)/a.u, Laplacian of electron density $\nabla^2\rho$ (r)/a.u, ratio $G(r)/V(r)$, energy density $H_{(r)}$/a.u at the BCP, E_{int}/Kcalmol^{-1}, ELF, and LOL in a.u.

Molecule	Bonding interaction	ρ (r)	$\nabla^2\rho$ (r)	$-G(r)/V(r)$®(r)	H (r)	E_{int}	ELF	LOL
A	M-N_{13}	0.071	0.261	0.841	−0.015	−29.719	0.165	0.302
	M-N_{32}	0.063	0.224	0.846	−0.012	−25.358	0.155	0.294
	M-S_{12}	0.037	0.093	0.845	−0.005	10.542	0.160	0.294
	M-S_{28}	0.054	0.013	0.792	−0.012	−18.016	0.203	0.329
	M-O_{14}	0.049	0.211	0.914	−0.006	−19.980	0.110	0.249
	M-0_{16}	0.071	0.311	0.880	−0.012	−32.094	0.143	0.282
	N_{37}-H_{17}	0.055	0.093	0.735	−0.013	−15.542	0.284	0.387
	N_{36}-H_{18}	—	—	—	—	—	—	—
B	M-N_{13}	0.071	0.255	0.836	−0.095	−29.719	0.169	0.307
	M-N_{32}	0.071	0.254	0.836	−0.016	−29.666	0.169	0.307
	M-S_{12}	0.048	0.137	0.828	−0.009	−16.440	0.161	0.298
	M-S_{28}	0.048	0.138	0.827	−0.009	−16.497	0.162	0.299
	M-O_{14}	0.056	0.273	0.912	−0.007	−26.030	0.099	0.241
	M-0_{16}	0.056	0.273	0.912	−0.007	−25.943	0.099	0.241
	N_{37}-H_{17}	—	—	—	—	—	—	—
	N_{36}-H_{18}	—	—	—	—	—	—	—
C	M-N_{13}	0.073	0.286	0.846	−0.016	−32.325	0.155	0.297
	M-N_{32}	0.073	0.285	0.846	−0.016	−32.319	0.155	0.297
	M-S_{12}	0.044	0.113	0.833	−0.007	−13.240	0.175	0.312
	M-S_{28}	0.044	0.113	0.833	−0.007	−13.247	0.175	0.312
	M-O_{14}	0.064	0.304	0.888	−0.011	−30.793	0.109	0.255
	M-0_{16}	0.064	0.304	0.888	−0.011	−30.796	0.109	0.255
	N_{37}-H_{17}	0.046	0.094	0.802	−0.008	−12.250	0.227	0.352
	N_{36}-H_{18}	0.046	0.094	0.802	−0.008	−12.241	0.227	0.351
D	M-N_{13}	0.086	0.292	0.798	−0.025	−38.435	0.193	0.328
	M-N_{32}	0.086	0.292	0.798	−0.025	−38.416	0.192	0.328
	M-S_{12}	0.016	0.036	0.943	−0.001	−3.203	0.083	0.231
	M-S_{28}	0.016	0.035	0.944	−0.001	−3.126	0.081	0.229
	M-O_{14}	0.077	0.333	0.846	−0.019	−37.796	0.134	0.281
	M-0_{16}	0.077	0.333	0.846	−0.019	−37.743	0.134	0.281
	N_{37}-H_{17}	0.058	0.094	0.720	−0.015	−16.801	0.300	0.396
	N_{36}-H_{18}	0.058	0.095	0.722	−0.015	−16.722	0.299	0.395
E	M-N_{13}	0.072	0.266	0.864	−0.013	−28.660	0.167	0.310
	M-N_{32}	0.072	0.269	0.863	−0.013	−29.090	0.168	0.310
	M-S_{12}	0.026	0.054	0.843	−0.003	−6.140	0.135	0.283
	M-S_{28}	0.024	0.050	0.846	−0.003	−5.680	0.129	0.278
	M-O_{14}	0.061	0.276	0.915	−0.007	−26.143	0.113	0.263
	M-0_{16}	0.061	0.278	0.915	−0.007	−26.246	0.113	0.263
	N_{37}-H_{17}	0.047	0.095	0.795	−0.008	−12.692	0.233	0.355
	N_{36}-H_{18}	0.047	0.095	0.794	−0.008	−12.709	0.233	0.356

ELF and LOL are the electron localization function and localized orbital locator, respectively.

B3BJ. The HOMO, LUMO, and energy gap (ΔE) are reported in Table 4.

The results show that the complexation of the ligand with transition metals led to a decrease in the HOMO and LUMO energies, thus causing a corresponding decrease in the energy gap. The decrease in the HOMO and LUMO energies are the highest in the Ni^{2+} and Fe^{2+} complexes and the lowest in the Fe^{2+} and Zn^{2+} complexes, and hence, the energy gap in the investigated molecules decreases in the order L > E > B > C > D > A. This observation may suggest that electrons can easily be promoted from the HOMO to the LUMO of the complexes, hence inducing charge transfer.

Figure 2 by inspection, shows a high concentration of HOMO on the thiophene and azomethine bond and less pronounced on the isoxazole moiety in the ligand. In almost all the complexes studied, the HOMO is widely spread on the ligand except in compound C where it is fully localized on the central metal atom.

In contrast, the LUMO is more pronounced on the thiophene moiety in the ligand and spreads over the entire molecule in the complexes. Thus, HOMO-LUMO transitions may be seen as electrons moving from ligand to ligand or central metal atom in most cases except for C with transitions from metal centres to ligands.

The distribution of electrons in the HOMO and LUMO was further supported by the density of state (DOS) analysis [58]. The DOS graphs of the ligand and the investigated complexes were aided by the GaussSum graphical tool [59] and are presented in Figure 3.

Table 4: Energies of HOMOs (E_{HOMO}), LUMOs (E_{LUMO}), and energy gap (ΔE) in eV calculated at M06-D3ZERO/def2-TZVP level of theory in the gas phase.

Chemical species	E_{HOMO}	E_{LUMO}	ΔE
L	−6.68	−2.13	4.55
$[Fe(L)_2(H_2O)_2]^{2+}$ (A)	−11.10	−10.02	1.07
$[Co(L)_2(H_2O)_2]^{2+}$ (B)	−12.74	−8.91	3.83
$[Ni(L)_2(H_2O)_2]^{2+}$ (C)	−13.05	−9.23	3.82
$[Cu(L)_2(H_2O)_2]^{2+}$ (D)	−13.02	−9.42	3.60
$[Zn(L)_2(H_2O)_2]^{2+}$ (E)	−13.01	−8.71	4.30

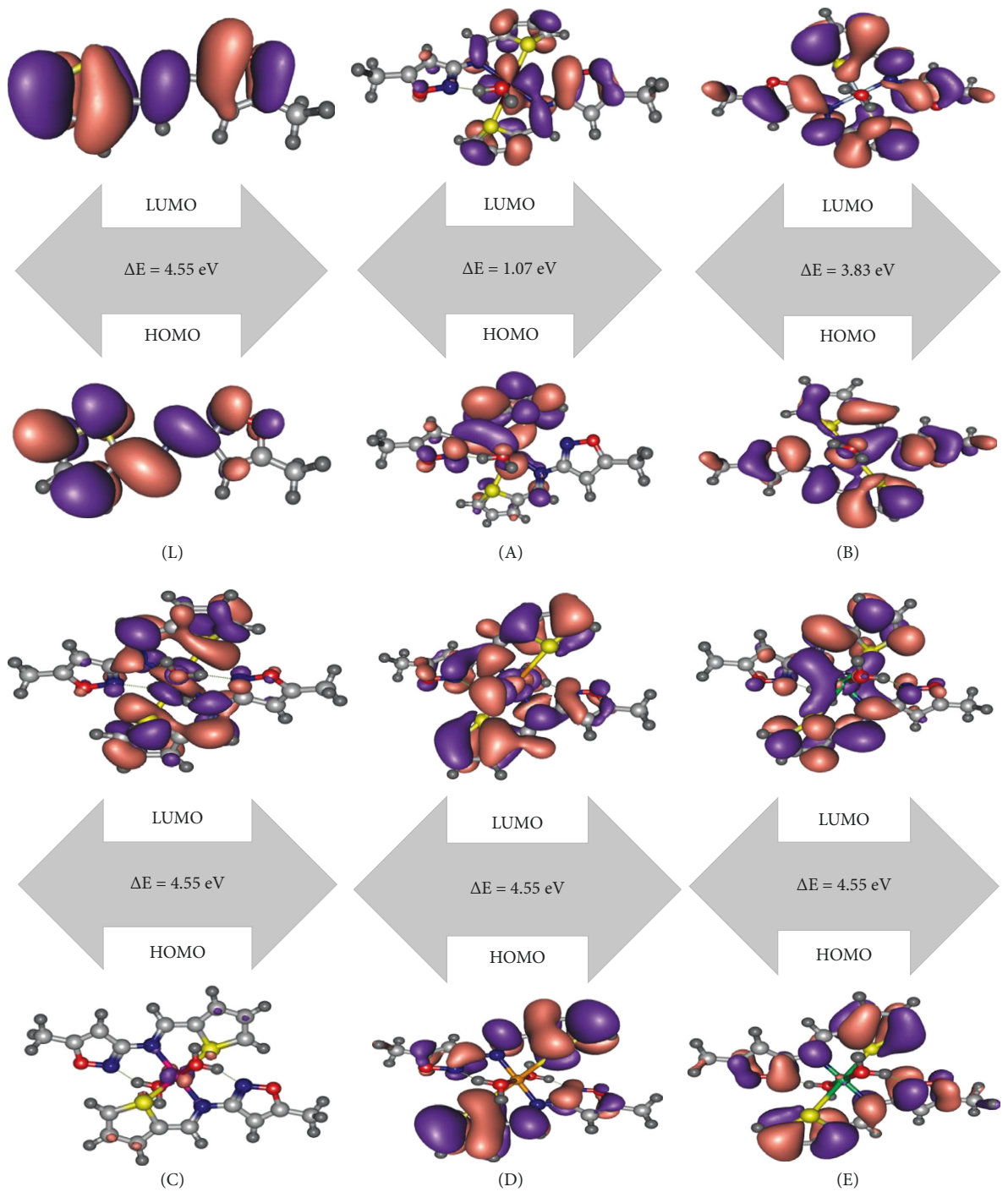

Figure 2: Gas-phase contour plots of HOMO and LUMO orbital diagrams of all investigated molecules at the M06/def2-TZVP/D3ZERO level of theory.

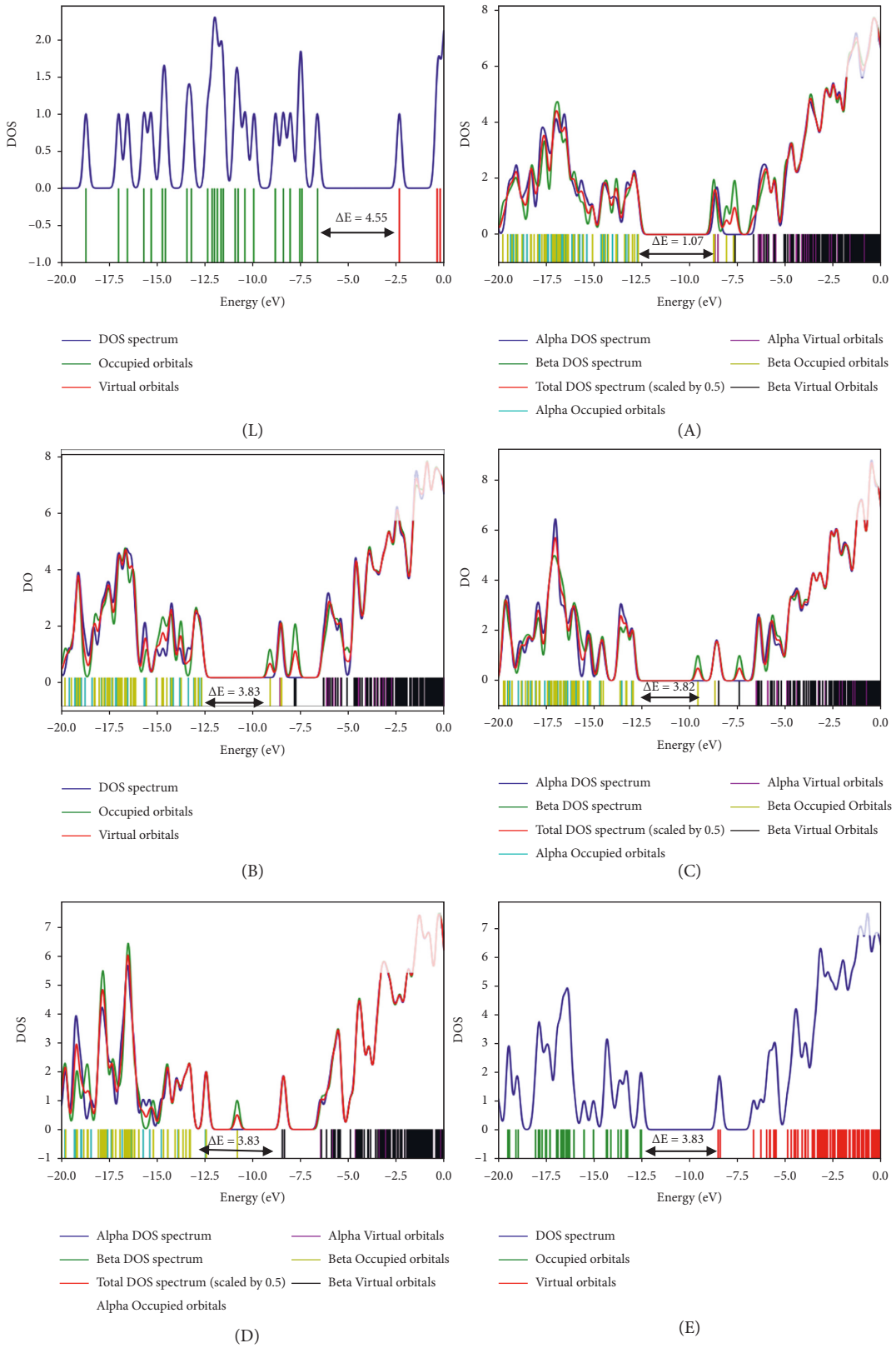

Figure 3: Density of state (DOS) plots of investigated chemical species.

Table 5: Adiabatic ionization potential (IP_a), electron affinity (EA_a), global hardness (η), softness (S), electronegativity (χ), chemical potential (μ), and electrophilicity (ω) in eV.

Chemical species	IP_a	EA_a	η	χ	μ	ω
L	7.83	0.77	3.532	4.300	−4.300	9.247
$[Fe(L)_2(H_2O)_2]^{2+}$ (A)	48.03	−28.21	38.121	9.908	−9.908	49.084
$[Co(L)_2(H_2O)_2]^{2+}$ (B)	13.84	7.90	2.972	10.869	−10.869	59.066
$[Ni(L)_2(H_2O)_2]^{2+}$ (C)	13.86	7.72	3.069	10.792	−10.792	58.232
$[Cu(L)_2(H_2O)_2]^{2+}$ (D)	13.61	9.65	1.979	11.629	−11.629	67.619
$[Zn(L)_2(H_2O)_2]^{2+}$ (E)	12.51	8.03	2.239	10.267	−10.267	52.710

The figure shows that transition metal complexation leads to a redistribution of electrons in the ligand, which can be observed by a significant decrease in the HOMO and LUMO energies. This induces an overall decrease in the energy gap as can be seen in the FMO diagrams of all the complexes. This observation shows that the decrease in the energy gap of the chemical species studied may suggest an improvement in the charge transfer within the molecules, which is in line with the FMO study.

3.2.2. Ionization Potential (IP), Electron Affinity (EA), and Global Reactivity Descriptors. The adiabatic IPs and EAs were obtained from SPE of the ground state and ionic species at the M06/def2-TZVP/D3ZERO level of theory. Because the molecular geometry may change upon leaving from neutral to ionic species, adiabatic values were considered in this study. From the IP and EA values, other global reactivity descriptor parameters were deduced as well and are reported in Table 5. IP measures the energy required to remove an electron in the ground state of an atom, while EA measures the energy released when a neutral species at the ground state accepts an electron [60]. Values of the adiabatic IP and EA are reported in Table 5.

It can be deduced from Table 5 that IP is greater than EA in all cases and follows the trend: A > C > B > D > E. This may be a possible suggestion that complex A with the highest IP has high electron releasing power and complex E with the least. On the other hand, complex D has the highest electron-accepting ability, while A has the least accepting power. EA follows the trend: D > E > B > C > A.

To gain insight into the chemical reactivity and stability of the molecules investigated, conceptual DFT was used. Global reactivity descriptors (GRDs) such as electronegativity (χ), global hardness (η), and electrophilicity index (ω) measure the chemical reactivity of a molecule as a whole. While the chemical potential (μ) is related to the measure of the electron's tendency to escape from a system at the ground state [61], the chemical hardness (η) on the other hand is an indicator of the overall stability of the system and measures the resistance of a molecule to intramolecular charge transfer [62]. Furthermore, electrophilicity (ω) is associated with the measurement of the stabilization energy when a system gets an additional electronic charge from an external environment [63, 64]. These parameters may be calculated, and their values are reported in Table 5.

Table 5 also shows that chemical hardness (η) follows the trend: A > L > C > B > E > D. It is clear from the ranking that metal complexation leads to a decrease in the chemical hardness except for A, suggesting a decrease in the resistance of electrons release for intermolecular charge transfer upon complexation. The chemical potential (μ) follows the order L > A > E > C > B > D, indicating that A is the most chemically reactive in terms of electron donation and Cu (II) complex most reactive in terms of electron acquisition. Moreover, one of the governing parameters for global reactivity studies is electrophilicity, which in this case follows a similar trend as compared to the chemical potential.

3.2.3. Local Reactivity Descriptors. Local reactivity descriptors are used to characterize the reactivity of molecular sites and all the individual atoms that constitute a molecule [65]. A detailed and explicit description of LRDs and GRDs can be found in [66]. In this study, the net charges were calculated using Hirshfeld population charge analysis to calculate the condensed Fukui functions. The donor (f_k^-), acceptor (f_k^+), and condensed Fukui functions for the compounds investigated are presented in Tables S7 and S8 of the ESM. These tables show that the azomethine bond in the ligand is characterized by a nucleophilic C atom (C1) ($f_k^- = 0.014$) and an electrophilic N_{13} ($f_k^+ = 0.159$). This fact is further supported by condense Fukui functions (Δf_k) values of −0.038 and 0.182, respectively. This evidence shows the likeness of the azomethine bond (C=N) to be approached by electrophiles and nucleophiles. On the other hand, the sulphur atom of the thiophene ring (S_{12}) may be regarded as a nucleophilic site as $\Delta f_k = -0.1102$ and hence prone to an attack by electrophiles. Moreover, the isoxazole nitrogen (N_{38}) is electrophilic ($f_k^+ = 0.126$) and susceptible to nucleophilic attack. Tables S7 and S8 equally show a reduction in the nucleophilic and electrophilic abilities of the azomethine carbons (C_1 and C_{21}) and nitrogens (N_{13} and N_{32}), respectively, upon complexation. This can be observed by a reduction in the concentration of charges around these atoms. Similarly, on average, the thiophene sulphur (S_{12} and S_{28}) is less nucleophilic. Also, the water molecules in the coordination sphere are characterized by electrophilic oxygens (O_{14} and O_{16}) and nucleophilic hydrogens (H_{15}, H_{17}, H_{18}, and H_{19}) associated with highly positive and negative values of f_k^+ and Δf_k, respectively.

3.2.4. Molecular Electrostatic Potential (MEP) Analysis. To further elucidate the reactive sites of the molecules studied, their MEP surfaces were computed at the RIJCOSX-M06/def2-TZVP level of theory and are displayed in Figure 4.

The different colours at the MEP surfaces, red to yellow, are indicative of regions of low electrostatic potential, which are characteristics of electrophilic sites, while green to blue is indicative of regions of high electrostatic potential, which are

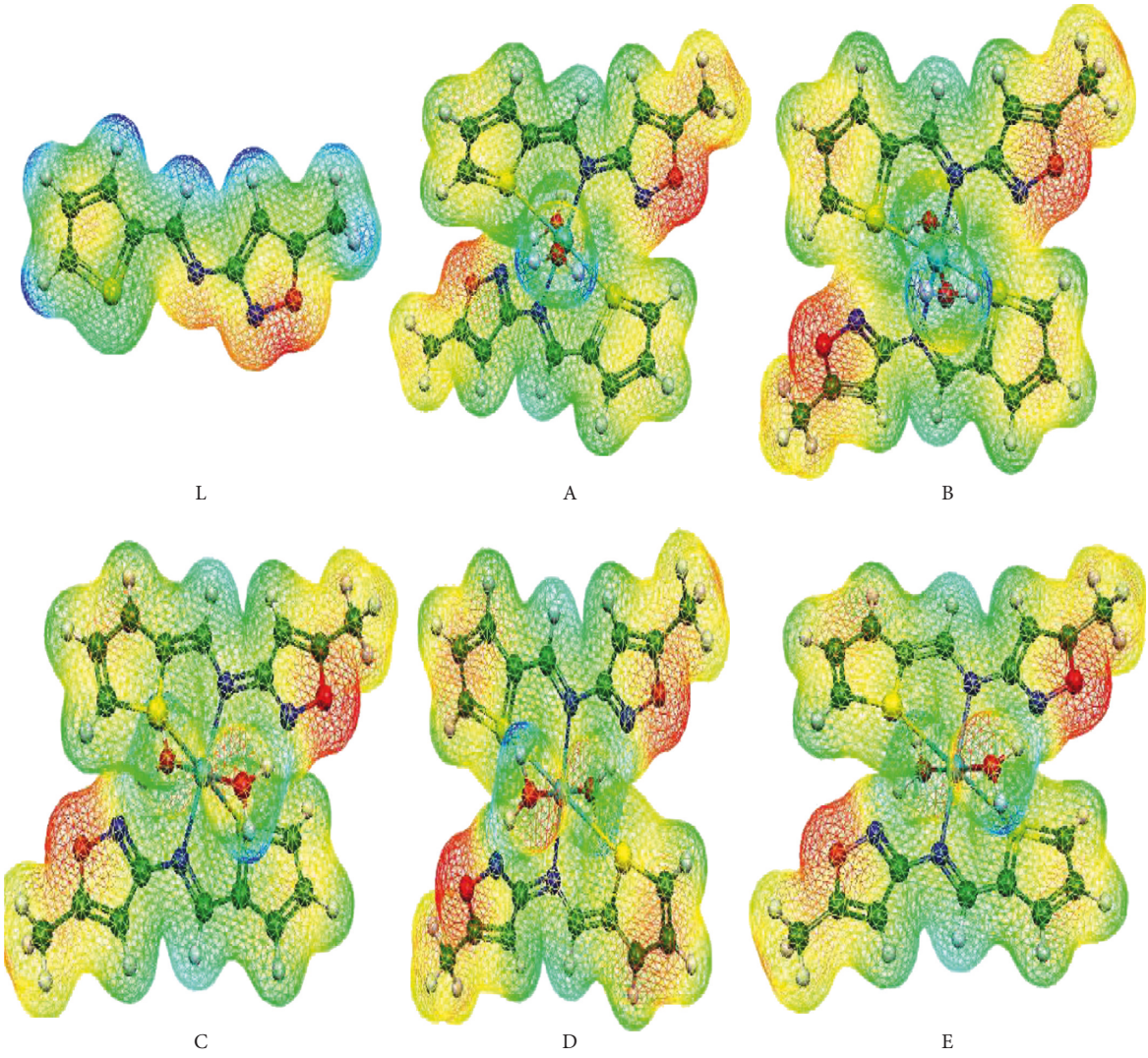

Figure 4: Calculated electrostatic potential surfaces for molecules studied. Regions of higher electron density are displayed in red and lower electron density in blue.

characteristics of nucleophilic sites. Figure 4 shows the isoxazole rings in general, where the O and N atoms, in particular, are the most susceptible to nucleophilic attacks. Moreover, all the H atoms of the isoxazole and thiophene rings of the ligand are acidic and favourable sites for electrophilic attacks. Upon complexation, a different scenario is observed as most H atoms become less acidic. The most nucleophilic sites in the investigated complexes are the H atoms of water molecules and that of the azomethine bond. Hence, these hydrogen atoms can likely take part in intra- and intermolecular hydrogen bonding with the molecule.

3.3. Charge Transfer Properties

3.3.1. Reorganization Energies, Charge Transfer Integrals, Rates, and Mobilities. IP and EA are important parameters in defining the mobilities of organic semiconductors. The mobilities and charge injection efficiency are important parameters that affect the performance of an OFET device [67, 68]. For suitable OFET materials, it suffices that the electrode materials have a work function capable of injecting holes and electrons into the HOMO and LUMO of semiconductor molecules. In this light, the organic semiconductor requires high electron affinity and low ionization potential enough to allow efficient injection of electrons and holes into empty LUMO and HOMO, respectively. Moreover, for high mobilities, the organic semiconductor requires low reorganization energies [37] and high charge transfer integrals with charge transfer rates being the governing factor. The reorganization energies and charge transfer integrals, as well as charge transfer rates and charge transfer mobilities, were calculated using M06/D3/def2-TZVP and PBE0/D3/def2-TZVP levels of theories, and their results are reported in Tables 6 and 7 respectively.

Analyses of Tables 6 and 7 indicate that transition metal complexation leads to a significant modification in the values of the reorganization energies, charge transfer integrals, charge transfer rates, and charge transfer mobilities of holes and electrons. The values of the reorganization

Table 6: Computed values of reorganization energies ($\lambda_{e/h}$) and charge transfer integrals ($V_{e/h}$) at the M06/D3/def2-TZVP and PBE0/D3/def2-TZVP level of theories in gas phase.

Species	λ_e (eV)		λ_h (eV)		V_e (eV)		V_h (eV)	
	M06	PBE0	M06	PBE0	M06	PBE0	M06	PBE0
L	0.2426	0.3130	0.4784	0.4431	0.1205	0.1247	0.0685	0.0723
A	0.4625	0.6023	0.8015	0.7648	0.3362	0.1976	1.0690	0.8016
B	0.3643	0.6176	0.0085	0.2102	1.2538	0.6380	0.1013	0.0676
C	0.2890	0.1825	0.1222	0.1197	0.2571	0.1715	0.4950	0.2223
D	1.6880	1.8137	0.6129	0.70287	0.1424	0.1001	0.0029	0.0006
E	0.7160	0.9767	1.3309	1.6800	0.0446	0.0506	0.6863	0.6881

Table 7: Computed values of charge transfer rates ($k_{e/h}$) and charge transfer mobilities ($\mu_{e/h}$) at the M06/D3/def2-TZVP and PBE0/D3/def2-TZVP levels of theories in the gas phase.

Species	k_e (s^{-1})		k_h (s^{-1})		μ_e ($cm^2 \cdot V^{-1}S^{-1}$)		k_h (s^{-1})	
	M06	PBE0	M06	PBE0	M06	PBE0	M06	PBE0
L	4.690×10^{13}	9.901×10^{13}	1.110×10^{12}	1.775×10^{12}	1.4591	3.0800	0.0350	5.5214
A	3.125×10^{13}	3.955×10^{13}	8.810×10^{12}	9.237×10^{13}	0.9722	1.2431	0.2740	2.8735
B	12.710×10^{14}	2.153×10^{14}	16.546×10^{14}	2.150×10^{13}	39.5401	6.6970	51.4740	6.6890
C	12.428×10^{13}	20.358×10^{13}	11.78×10^{15}	7.543×10^{14}	3.8660	6.3330	366.4740	23.4650
D	1.9288×10^{7}	2.700×10^{4}	4.984×10^{8}	7.820×10^{8}	0.0000	0.0000	0.0000	0.0000
E	3.8110×10^{10}	3.294×10^{9}	1.644×10^{10}	4.890×10^{8}	0.0010	0.0001	0.0010	0.0000

energies and charge transfer integrals calculated at the M06/D3/def2-TZVP are similar to those obtained using the PBE0/D3/def2-TZVP method though with slight disparity in their trend (see Table 6). Similar observations have been made for the charge transfer rates and mobilities with the PBE0/D3/def2-TZVP method in most cases showing an increase in the values of $\lambda_{e/h}$ and $V_{e/h}$ and a somewhat opposite effect on the corresponding $k_{e/h}$ and $\mu_{e/h}$ values. However, discussions of result in this work is solely based on the former as the M06 functional contains more Hartree–Fock (HF) exchange (27%) and is more appropriate for energy calculations of transition metal complexes [37] as compared to the latter with 25% HF exchange. For comparison, tris(8-hydroxyquinolinato) aluminium (Alq_3) ($\lambda_e = 0.276$ eV) [37, 69] and N-N′-diphenyl-N-N′-bis(3-methylphenyl-(1,1′-biphyl)-4,4′-diamine (TPD) ($\lambda_h = 0.290$ eV) [37, 70] were considered reference molecules for electrons and holes reorganization energies, respectively.

The predicted λ_e and λ_h values vary in the order D > E > A > B > C > L and E > A > D > L > C > B, respectively. This may suggest that the ligand and B with $\lambda_e = 0.2426$ eV and $\lambda_h = 0.0085$ eV, respectively, are potential contestants for electron and hole-transport materials as their reorganization energies are smaller relative to that of the reference molecules and therefore possess the highest charge transfer rates and mobilities as expected. Meanwhile, the electron (μ_e) and hole (μ_e) charge transfer mobilities follow the order: B > C > L > A > E > D and C > B > A > L > E > D with B and C having the highest electron and hole mobilities, respectively (see Table 7). Moreover, the respective values of electron and hole mobilities of B (39.5401 $cm^2 \cdot V^{-1}S^{-1}$) and C (366.4740 $cm^2 \cdot V^{-1}S^{-1}$) are remarkably larger than those of the ligand. These results further ascertain the modification of charge transfer properties upon complexation. Hence, based on charge transfer mobilities, B and C are outstanding with good electron and hole-transporting properties. Compound B has a good balance between electron and hole mobilities and may serve as a good ambipolar transport material, while compound C has a remarkable hole mobility and can be exploited as a hole-transporting material. Hence, compounds B and C may stand as promising molecules for the manufacture of electrons and hole-transport layer materials highly employed in the construction of OLED and OFET devices. This observation further suggest that the charge transport properties of organic systems may be fine-tuned by transition metal complexation.

3.4. Absorption Spectra. To gain insight into the electronic transition of the compounds investigated in the gas phase, quantum calculations employing the time-dependent density functional theory (TD-DFT) at the PBE0/D3BJ/ma-def2-TZVP/def2/J level of theory were performed. To predict the electronic absorption spectra of the compounds, transitions to the first 20 excited states were calculated where the dominant transitions with the highest oscillator strengths were considered (as presented in Table 8), and the simulated UV-visible absorption spectra of the investigated compounds are depicted in Figure S3. This table presents the absorption wavelength (λ_{max}), oscillator strength (f), and the main assignment, as well as the vertical excitation energies (E_{ex}). Inspection of Table 7 shows that complexation leads to an increase in the wavelength (redshift). Moreover, the λ_{max} and f values of the two most intense excitations of E are similar to that of the ligand though having slight bathochromic shifts. This may suggest that the substitution of the central metal ion by Zn^{2+} does not affect the absorption spectra significantly.

Table 8: Absorption spectra data obtained by TD-DFT methods for studied compounds at PBE0/D3BJ/ma-def2-TZVP/def2/J level in the gas phase.

Chemical species	Transition	λ_{max} (nm)	f	Assignment	E_{ex} (eV)	S_r (Å)	D_{index} (Å)	t_{index} (Å)	H_{index} (Å)
L	$S_0 \longrightarrow S_1$	308.1	0.637	$H \longrightarrow L$	4.025	0.759	0.360	−1.368	2.801
A	$S_0 \longrightarrow S_8$	389.0	0.004	$H_b \longrightarrow L_b$	3.187	0.467	2.933	0.918	3.058
B	$S_0 \longrightarrow S_9$	449.8	0.031	$H_b \longrightarrow L_b$	2.757	0.448	0.021	−2.006	2.948
C	$S_0 \longrightarrow S_{20}$	330.2	0.028	$H_a \longrightarrow L_a$	3.754	0.543	0.092	−2.380	3.382
D	$S_0 \longrightarrow S_{17}$	407.9	0.092	$H_b - 1 \longrightarrow L_b + 1$	3.039	0.528	0.001	−1.517	2.618
E	$S_0 \longrightarrow S_4$	324.3	0.595	$H \longrightarrow L + 1$	3.823	0.660	0.002	−2.687	4.004

a and b represent contributions from alpha and beta orbitals, respectively.

3.5. Electron Excitation Analysis. Here, the molecular orbitals from TD-DFT calculations were used while employing its output files and that of Molden generated by ORCA. Upon the absorption of a photon in a semiconductor device, there is the excitation of electrons from the valence band to the conduction band, leading to the creation of holes in the valence band [71, 72]. This can equally be regarded as a HOMO-LUMO transition, whereby electrons are promoted to the LUMO while creating holes in the HOMO. Excitations may be classified as local or charge transfer (CT) excitations. In the former, electrons and holes occupy similar spatial regions, while in the latter, they occupy different spatial leading to the substantial displacement of charge density and hence charge transfer [73].

Hence, to characterize the nature of excitation and the electron-hole distribution in the studied chemical species, some important parameters were considered. These parameters include the overlap function between the hole and electron distribution (S_r), the magnitude of charge transfer length (D_{index}), the overall measure of the degree of the spatial extension of the hole and electron distribution in the charge transfer direction (H_{index}), and the separation degree of hole and electron in the charge transfer direction (t). Generally, values of $t_{index} > 0$ imply there is a substantial separation of holes and electrons else not separated [73–75]. The values of these parameters are reported in Table 7, and the hole-electron distribution maps are depicted in Figure 5.

The figure shows a high degree of overlap between holes and electrons in the ligand as they widely spread over the entire molecule specifically on O and N (of the isoxazole ring), S (thiophene ring), and N (azomethine bond), respectively. By combining hole-electron maps and the indices, it can be deduced that the ligand excitation $S_0 \longrightarrow S_1$ may be regarded as a CT excitation characterized by large values of S_r (0.759 Å) and D_{index} (0.360 Å) [76] as reported in Table 8.

Additionally, the large values of the H_{index} of the excitation $S_0 \longrightarrow S_1$ (see Table 8) is as a result of the widespread of holes and electrons over the entire molecule (ligand). Moreover, the electron-hole distribution map for ligand shows that electrons and holes occupy different spatial regions, hence suggesting a CT excitation for this transition. Similar observations were made in all the complexes studied with a larger degree of separation of electrons and holes in space, suggesting even better charge transfer in the complexes. Furthermore, it can be seen that complexation leads to a drastic drop in the overlap (S_r) between hole and electrons and the magnitude of the charge transfer length (D_{index}). All D_{index} in the complexes is small (except for Fe, $S_0 \longrightarrow S_8$), while S_r indices are on average large. Also, all t values are negative (except for complex A) indicating that some electrons and holes may still occupy the same region. This may be associated with the somewhat symmetric nature of the investigated molecules, and thus, charge transfer is multidirectional.

For the $S_0 \longrightarrow S_{20}$ excitation in C, electrons are highly localized on the azomethine bond with little contribution from the thiophene ring, while holes on the other hand have a contribution from the central metal, water molecules, and azomethine bond. This may serve as plausible evidence of charge transfer involving metal centres. A similar situation is observed in all the other complexes with big or small contributions from metal centres to hole-electron distribution. It is important to note that in D and E, there are little or no contributions from metal centres, respectively, as hole-electron distribution is mainly localized on the ligand, and hence, very low charge transfer mobilities have been observed. This suggests that in these complexes, charge transfer mobilities are greatly influenced by charge transfers involving metal centres. Hence, from the table, it is evident that although the nature of excitation may not be directly related to the charge transfer mobilities of the studied compounds, excitation involving metal centres significantly improves the charge transfer mobilities of the studied compounds.

3.6. Nonlinear Optical (NLO) Properties. In this study, the effect of complexation on the static and dynamic NLO response on the parent molecular framework (L) was equally investigated. The static mean polarizability ($\langle\alpha\rangle$), the total static first hyperpolarizability (β_{tot}), the vector component of the first hyperpolarizability (β_{vec}), and the average second hyperpolarizability (γ) are calculated based on the following equations:

$$\langle\alpha\rangle = \frac{1}{3}\left(\alpha_{xx} + \alpha_{yy} + \alpha_{zz}\right), \tag{19}$$

$$\beta_{tot} = \left(\beta_x^2 + \beta_y^2 + \beta_z^2\right)^{1/2}, \tag{20}$$

where $\beta_x = (\beta_{xxx} + \beta_{xyy} + \beta_{xzz})$; $\beta_y = (\beta_{yyy} + \beta_{yzz} + \beta_{yxx})$;

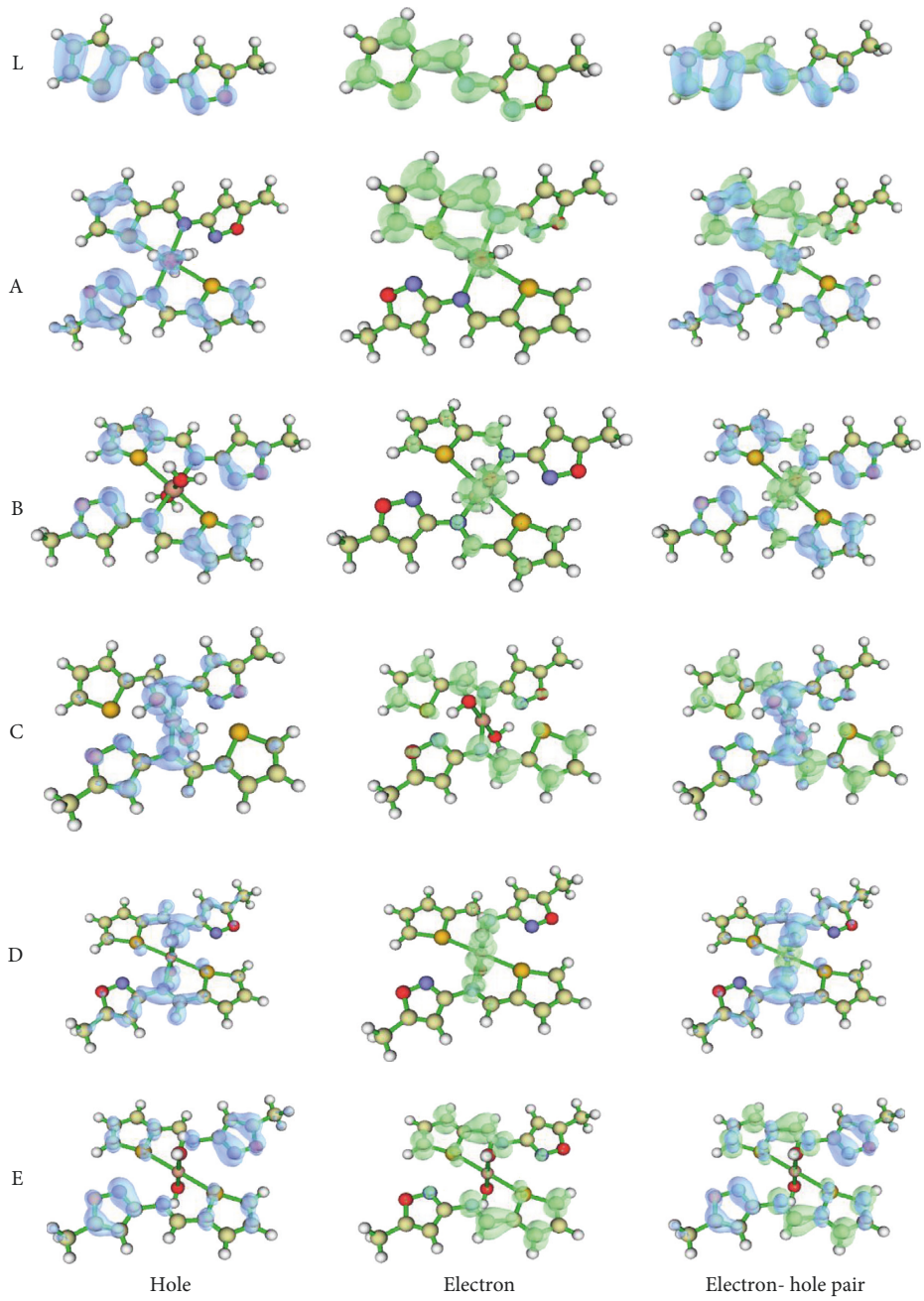

Figure 5: Hole-electron distribution maps of L, B, and C; the blue and green colours represent holes and electrons, respectively.

$$\beta_z = \left(\beta_{zzz} + \beta_{zxx} + \beta_{zyy}\right),$$
$$\beta_{\text{vec}} = \left(\beta_x{}^2 + \beta_y{}^2 + \beta_x{}^2\right)^{1/2}, \quad (21)$$

where $\beta_i (i = x, y, z)$ is given by

$$\beta_i = \left(\frac{1}{3}\right) \sum_{j=x.y.z} \left(\beta_{ijj} + \beta_{jij} + \beta_{jji}\right), \quad (22)$$

$$\langle \gamma \rangle = \frac{1}{5}\left(\gamma_{xxxx} + \gamma_{yyyy} + \gamma_{zzzz} + 2\gamma_{xxyy} + 2\gamma_{xxzz} + 2\gamma_{yyzz}\right). \quad (23)$$

The values of the static mean polarizability (α (0; 0)), static first hyperpolarizability (β (0; 0, 0)), and the static second hyperpolarizability (γ (0; 0, 0, 0)), and their frequency-dependent NLO properties were determined at the wB97X-D/6-311++G level of theory. The range-separated functional wB97X-D was used since the range-separated exchange renders them more appropriate for the calculation NLO properties [77]. All calculations related to the NLO properties have been carried out using the Gaussian 09 software [78], and related values are reported in Tables 9–13. The conversion factors between atomic units and electrostatic units (esu) have been used as $1\,\text{a.u.} = 0.5 \times 10^{-24}$ electrostatic units (esu) for static polarizability,

Table 9: Static average isotropic polarizabilities ($\langle\alpha\rangle$) alongside some of its components for L, transition metal complexes, and p-NA, calculated at $\omega = 0$ at the wB97xd/6-311++G level of theory.

Species	α_{xx}	α_{yx}	α_{yy}	α_{zx}	α_{zy}	α_{zz}	$\langle\alpha\rangle \times 10^{-22}$ esu
L	211.89	−49.90	161.96	0.26	0.02	75.02	2.22
A	379.22	−39.49	311.10	65.46	−23.34	251.83	4.65
B	290.10	−70.00	278.06	51.14	−10.35	152.55	3.56
C	329.09	−132.83	280.96	16.17	−44.37	307.78	4.53
D	378.73	−18.05	310.22	109.73	−90.63	271.71	4.75
E	438.24	66.00	313.49	15.94	−41.53	181.96	4.61
p-NA	49.16	−20.17	98.07	−11.43	−492.41	144.07	1.44

Table 10: Total static average first hyperpolarizabilities (β_{tot}) alongside some of its components for L, transition metal complexes, and p-NA, calculated at $\omega = 0$ at the wB97xd/6-311++G level of theory.

Species	β_{xxx}	β_{yyy}	β_{zzz}	β_x	β_y	β_z	$\beta_{tot} \times 10^{-31}$ esu
L	570.02	54.45	−0.86	1846.13	−575.21	27.75	167.08
A	227.10	82.59	196.64	898.67	135.35	1292.29	136.49
B	0.231	−3.738	−0.001	1.422	−4.253	−0.010	38.74
C	−0.12	3.69	0.07	−0.74	0.36	0.29	0.07
D	0.003	1.50	2.93	9.29	−7.21	10.54	1.36
E	−7.10	4.05	−0.17	−35.93	−6.20	4.91	3.18
p-NA	−5.53	−20.20	−1869.94	685.67	4.14	−5062.73	441.38

Table 11: Total static average second hyperpolarizabilities ($\langle\gamma\rangle$) alongside some of its components for ligand, transition metal complexes, and p-NA, calculated at $\omega = 0$ at the wB97xd/6-311++G level of theory.

Species	γ_{xxxx}	γ_{yyyy}	γ_{zzzz}	γ_{xxyy}	γ_{xxzz}	γ_{yyzz}	$\langle\gamma\rangle \times 10^{-35}$ esu
L	170216.00	30067.10	16564.10	−45559.20	8425.45	7730.04	1.59
A	149721.00	73022.90	51336.50	34998.40	37425.60	17165.30	4.57
B	−98196.60	362035.00	65901.61	−120.70	−120.71	−587.20	3.31
C	67306.10	63713.10	68945.50	41197.60	25898.70	33808.10	4.05
D	116850.00	35176.60	41211.60	29410.40	37492.40	17671.80	3.65
E	184082.00	48635.00	21773.00	27534.90	11170.80	8755.63	3.52
p-NA	10364.90	10020.20	120405.10	4647.18	5024.00	−1357.10	1.59

Table 12: Values of selected components of the frequency-dependent first hyperpolarizability, calculated at $\omega = 0.04282$ a.u (1064 nm) at the wB97xd/6-311++G level of theory.

Species	β_{xxx}	β_{yyy}	β_{zzz}	β_x	β_y	β_z	$\beta_{vec} \times 10^{-31}$ esu
L	873.29	40.43	−0.01	2879.06	−0.0001	39.74	248.76
A	451.92	112.46	253.23	1672.53	−23.74	1622.37	201.32
B	−1.163	4.487	0.002	−4.919	6.924	−1.563	74.61
C	−0.16	0.10	0.11	−1.02	0.75	0.57	0.12
D	−1.18	1.26	3.60	5.44	−18.12	17.13	2.21
E	−8.96	−0.79	−1.48	51.89	−43.62	−2.02	5.86
p-NA	−6.37	−23.83	−2964.70	1092.88	6.511	−8271.56	720.83

Table 13: Average values of frequency-dependent first and second hyperpolarizabilities (in a.u.) corresponding to some NLO properties of ligand and its transition metal complexes, calculated at frequency $\omega = 0.04282$ a.u. at the wB97XD/6-311++G level of theory.

NLO property	L	A	B	C	D	E	p-NA
SHG ($(-2\omega; \omega, \omega)$)	609.73	466.05	1.87	0.28	5.10	13.56	1668.69
EOPE (β $(-\omega; \omega, 0)$)	434.97	352.18	1.75	0.22	3.73	9.94	1182.45
THG (γ $(-3\omega; \omega, \omega, \omega)$)	76689.10	100955.00	71190.60	88208.80	81461.60	78885.70	37284.30
EFISHG ($(-2\omega; \omega, \omega, 0)$)	100647.00	132708.00	26216.91	115765.00	104969.00	102025.00	54826.20

1 a.u. = 8.639418×10^{-33} electrostatic units (esu) for first hyperpolarizability (β), and 1 a.u. = 0.50367×10^{-39} esu for second hyperpolarizability (γ) [37]. The analysis of the results shows that the coordination of L to the different transition metal centres results in a significant increase in the values of α (0; 0) and γ (0; 0, 0, 0), but in contrast, a decrease in β (0; 0, 0) is observed. Besides, the ligand and its transition metal complexes have α (0; 0) and γ (0; 0, 0, 0) values larger than those of p-NA (see Tables 9–11). Thus, suggesting that all the investigated molecules are potential candidates for third-order NLO applications. Table 10 shows a drastic drop in the β (0; 0, 0) values upon coordination to transition metal. This observation may be related to the fact that the dominant components of β (0; 0, 0) are from β_x and β_{xxx} in ligand, suggesting that charge transfer occurs primarily in the x-direction where majority of the π-conjugated framework lies. In the complexes, the dominant components are from multiple directions with little or negative contributions from β_x and β_{xxx} components.

Also, the vector component of the first hyperpolarizability (β_{vec}) alongside some NLO frequency-dependent properties were computed at the typical Nd: YAG laser frequency of 0.04282 a.u. (corresponding to the wavelength (λ) = 1064 nm) and are reported in Tables 4 and 5. Analysis of Table 4 shows that the ligand and its complexes have lower values of β_{vec} as compared to p-NA and that upon complexation of L, there is a significant decrease in β_{vec}. Similar observations were made with the frequency-dependent NLO response including SHG and EOPE based on the static first hyperpolarizabilities. In contrast, all the investigated molecules show remarkably large second hyperpolarizabilities frequency-dependent NLO response (THG and EFISHG) compared to p-NA, with improved properties upon complexation. These results therefore shows that L and its metal complexes may stand as potential candidate materials for the manufacture of optoelectronic devices for applications in OLEDs and OFETs.

4. Conclusion

In this work, the structural and electronic properties of an isoxazole derivative have been investigated. QTAIM analysis using Bader's approach showed the partly covalent nature of all ligand to metal bonds with the presence of H-bonding and weak interligand interactions. All complexes showed octahedral geometries. Reactivity studies showed that thiophene sulphur and azomethine carbon are nucleophilic sites prone to electrophilic attacks, while azomethine nitrogen and water O are electrophilic and are thus susceptible to nucleophilic attacks. Compounds A and D seem to be the most and least resistant in releasing their electrons for intermolecular charge transfer, respectively, hence characterized by low charge transfer rates and mobilities. Similarly, compounds B and A are most and least chemically reactive in terms of electron donation, respectively. To gain insight into the charge transfer potential of the investigated molecules, reorganization energies (λ), charge transfer integrals (V), charge transfer rates (K_{CT}), and charge transfer mobilities (μ) were calculated at M06-D3ZERO/def2-TZVP/RIJCOSX. Conclusively, the Co^{2+} and Ni^{2+} complexes, and the ligand are good electron carriers, while Ni^{2+} and Co^{2+} complexes are good hole transporters, highly demanded in the manufacture of OFETs and OLEDs. Moreover, the Co^{2+} complex has electron and hole-transport properties and hence can be employed as an ambipolar molecule though having dominant hole-transporting properties. Also, all the investigated molecules show improved static and dynamic second hyperpolarizabilities properties upon complexation and with values comparatively higher than those of para-nitroaniline (p-NA). From the aforementioned results, it is evident that metal complexation greatly influences the charge transfer properties of organic molecules.

Data Availability

The data used to support the findings of this study are available from the corresponding author upon request.

Conflicts of Interest

The authors declare that there are no conflicts of interest regarding the publication of this article.

Acknowledgments

The authors acknowledge the support of the Research Unit of Noxious and Environmental Engineering (RUNOCHEE), Department of Chemistry, Faculty of Science, University of Dschang, Cameroon.

Supplementary Materials

Figure S1: Gas-phase optimized geometries of investigated molecules. Figure S2: Molecular graphs of L complexes based on their gas-phase optimized geometries. Figure S3: Simulated UV-visible absorption spectrum L and its complexes at the PBE0-D3/ma-def2-TZVP level of theory. Table S1: Computed values of the condensed Fukui functions (f_k^-, f_k^+) and the dual descriptor (Δf_k) in a.u. for L and complexes A and B. Table S2: Computed values of the condensed Fukui functions (f_k^-, f_k^+) and the dual descriptor (Δf_k) in a.u. for complexes C, D, and E. Table S3: Cartesian coordinates of the gas-phase optimized geometry of (L). Table S4: Cartesian coordinates of the gas-phase optimized geometry of complex A. Table S5: Cartesian coordinates of the gas-phase optimized geometry of complex B. Table S6: Cartesian coordinates of the gas-phase optimized geometry of complex C. Table S7: Cartesian coordinates of the gas-phase optimized geometry of complex D. Table S8: Cartesian coordinates of the gas-phase optimized geometry of complex E. (*Supplementary Materials*)

References

[1] M. K. Wei, C. W. Lin, C. C. Yang, Y. W. Kiang, J. H. Lee, and H. Y. Lin, "Emission characteristics of organic light-emitting diodes and organic thin-films with planar and corrugated structures," *International Journal of Molecular Sciences*, vol. 11, no. 4, pp. 1527–1545, 2010.

[2] E. Di Mauro, D. Rho, and C. Santato, "Biodegradation of bio-sourced and synthetic organic electronic materials towards green organic electronics," *Nature Communications*, vol. 12, no. 1, p. 3167, 2021.

[3] A. Zvezdin, E. Di Mauro, D. Rho, C. Santato, and M. Khalil, "En route toward sustainable organic electronics," *MRS Energy & Sustainability*, vol. 7, no. 1, p. E16, 2020.

[4] C. H. Lin, S. Chattopadhyay, C. W. Hsu et al., "Enhanced charge separation by sieve-layer mediation in high-efficiency inorganic-organic solar cells," *Advanced Materials*, vol. 21, no. 7, pp. 759–763, 2009.

[5] J. T. Kim, J. Lee, S. Jang et al., "Solution processable small molecules as efficient electron transport layers in organic optoelectronic devices," *Journal of Materials Chemistry*, vol. 8, no. 27, Article ID 13508, 2020.

[6] T. Hirano, K. Matsuo, K. Kohinata et al., "Novel laser transfer technology for manufacturing large sized OLED displays," *SID Symposium Digest of Technical Papers*, vol. 38, no. 1, pp. 1592–1595, 2007.

[7] A. N. B. Sokolov, B. C. K. Tee, C. J. Bettinger, J. B. H. Tok, and Z. Bao, "Chemical and engineering approaches to enable organic field-effect transistors for electronic skin applications," *Accounts of Chemical Research*, vol. 45, no. 3, pp. 361–371, 2012.

[8] J. Zhuang, W. Li, W. Su, M. Zhou, and Z. Cui, "Novel ternary bipolar host material with carbazole, triazole and phosphine oxide moieties for high efficiency sky-blue OLEDs," *New Journal of Chemistry*, vol. 38, no. 2, pp. 650–656, 2014.

[9] V. Coropceanu, J. Cornil, D. A. Da Silva Filho, Y. Olivier, R. Silbey, and J. L. Brédas, "Charge transport in organic semiconductors," *Chemical Reviews*, vol. 107, no. 4, pp. 926–952, 2007.

[10] S. Revoju, A. Matuhina, L. Canil et al., "Structure-induced optoelectronic properties of phenothiazine-based materials," *Journal of Materials Chemistry C*, vol. 8, no. 44, Article ID 15506, 2020.

[11] E. L. Wehry, *Effects of Molecular Structure on Fluorescence and Phosphorescence*, Taylor & Francis, New York, NY, USA, 2nd edition, 1990.

[12] B. Valeur and M. N. Berberan-santos, *Molecular Fluorescence Principles and Applications*, Wiley-VCH, Weinheim, Germany, 2012.

[13] C. Kim, A. Facchetti, and T. J. Marks, "Gate dielectric microstructural control of pentacene film growth mode and field-effect transistor performance," *Advanced Materials*, vol. 19, no. 18, pp. 2561–2566, 2007.

[14] S. Arulmozhi, M. Victor, R. Antony, and J. Madhavan, "HOMO, LUMO analysis and first order hyperpolarizability of 2-amino-5-chloro benzophenone using computational methods," *Der Chemica Sinica*, vol. 2, p. 158, 2011.

[15] N. N. Ayare, V. K. Shukla, and N. Sekar, "Charge transfer and nonlinear optical properties of anthraquinone D-π-A dyes in relation with the DFT based molecular descriptors and perturbational potential," *Computational and Theoretical Chemistry*, vol. 1174, Article ID 112712, 2020.

[16] F. Neese, "The ORCA program system," *Wiley Interdisciplinary Reviews, Computational Molecular Science*, vol. 2, pp. 73–78, 2012.

[17] N. K. Nkungli, S. N. Tasheh, A. D. T. Fouegue, F. K. Bine, and J. N. Ghogomu, "Theoretical insights into the direct radical scavenging activities of 8-hydroxyquinoline: mechanistic, thermodynamic and kinetic studies," *Computational and Theoretical Chemistry*, vol. 1198, Article ID 113174, 2021.

[18] M. D. Hanwell, D. E. Curtis, D. C. Lonie, T. Vandermeersch, E. Zurek, and G. R. Hutchison, "Avogadro: an advanced semantic chemical editor, visualization, and analysis platform," *Journal of Cheminformatics*, vol. 4, no. 1, pp. 17–33, 2012.

[19] J. P. Perdew, "Density-functional approximation for the correlation energy of the inhomogeneous electron gas," *Physical Review B*, vol. 33, no. 12, pp. 8822–8824, 1986.

[20] F. Weigend and R. Ahlrichs, "Balanced basis sets of split valence, triple zeta valence and quadruple zeta valence quality for H to Rn: design and assessment of accuracy," *Physical Chemistry Chemical Physics*, vol. 7, no. 18, pp. 3297–3305, 2005.

[21] F. Neese, "Prediction of molecular properties and molecular spectroscopy with density functional theory: from fundamental theory to exchange-coupling," *Coordination Chemistry Reviews*, vol. 253, no. 5-6, pp. 526–563, 2009.

[22] F. Neese, "An improvement of the resolution of the identity approximation for the formation of the Coulomb matrix," *Journal of Computational Chemistry*, vol. 24, no. 14, pp. 1740–1747, 2003.

[23] S. Grimme, S. Ehrlich, and L. Goerigk, "Effect of the damping function in dispersion corrected density functional theory," *Journal of Computational Chemistry*, vol. 32, no. 7, pp. 1456–1465, 2011.

[24] Y. Zhao and D. G. Truhlar, "The M06 suite of density functionals for main group thermochemistry, thermochemical kinetics, noncovalent interactions, excited states, and transition elements: two new functionals and systematic testing of four M06-class functionals and 12 other functionals," *Theoretical Chemistry Accounts*, vol. 120, no. 1–3, pp. 215–241, 2008.

[25] L. Wang, T. Li, Y. Shen, and Y. Song, "A theoretical study of the electronic structure and charge transport properties of thieno [2,3-b] benzothiophene based derivativesb] benzothiophene based derivatives," *Physical Chemistry Chemical Physics*, vol. 18, no. 12, pp. 8401–8411, 2016.

[26] L. Wang, J. Dai, and Y. Song, "The substituent effect on the photophysical and charge transport properties of non-planar dibenzo[a,m] rubicenes," *New Journal of Chemistry*, vol. 45, Article ID 20556, , 2021.

[27] R. G. Parr and W. Yang, "Density functional approach to the frontier-electron theory of chemical reactivity," *Journal of the American Chemical Society*, vol. 106, no. 14, pp. 4049-4050, 1984.

[28] W. Yang and W. J. Mortier, "The use of global and local molecular parameters for the analysis of the gas-phase basicity of amines," *Journal of the American Chemical Society*, vol. 108, no. 19, pp. 5708–5711, 1986.

[29] C. Morell, A. Grand, and A. Toro-Labbé, "New dual descriptor for chemical reactivity," *The Journal of Physical Chemistry A*, vol. 109, no. 1, pp. 205–212, 2005.

[30] D. Chakraborty and P. K. Chattaraj, "Conceptual density functional theory based electronic structure principles," *Chemical Science*, vol. 12, no. 18, pp. 6264–6279, 2021.

[31] T. Lu and F. Chen, "Multiwfn: a multifunctional wavefunction analyzer," *Journal of Computational Chemistry*, vol. 33, no. 5, pp. 580–592, 2012.

[32] R. A. Marcus, "Electron transfer reactions in chemistry: theory and experiment (nobel lecture)," *Angewandte Chemie International Edition in English*, vol. 32, no. 8, pp. 1111–1121, 1993.

[33] M. Qiu, W. Pei, Q. Lu, Z. Li, Y. Li, and J. Liang, "DFT characteristics of charge transport in DBTP based hole

transport materials," *Applied Sciences*, vol. 9, no. 11, p. 2244, 2019.

[34] Y. X. Zhang, X. Cai, Y. Z. Ban, X. Y. Li, and J. Z. Jiang, "Density functional theory study on organic semiconductor for field effect transistors: symmetrical and unsymmetrical porphyrazine derivatives with annulated 1,2,5-thiadiazole and 1, 4-diamyloxybenzene moieties," *Journal of Physical Chemistry C*, vol. 112, p. 5148, 2008.

[35] V. Coropceanu, H. Li, P. Winget, L. Zhu, and J. L. Brédas, "Electronic-structure theory of organic semiconductors: charge-transport parameters and metal/organic interfaces," *Annual Review of Materials Research*, vol. 43, no. 1, pp. 63–87, 2013.

[36] M. Ajdari, T. Schmitt, M. Hoffmann et al., "Electronic properties of 6,13-diazapentacene adsorbed on Au (111): a quantitative determination of transport, singlet and triplet states, and electronic spectra," *Journal of Physical Chemistry C*, vol. 124, no. 24, Article ID 13205, 2020.

[37] C. H. A. Alongamo, N. K. Nkungli, and J. N. Ghogomu, "DFT-based study of the impact of transition metal coordination on the charge transport and nonlinear optical (NLO) properties of 2-{[5-(4-nitrophenyl)-1, 3, 4-thiadiazol-2-ylimino]methyl}phenol," *Molecular Physics*, vol. 117, no. 18, pp. 2577–2592, 2019.

[38] V. Lemaur, M. Steel, D. Beljonne, J. L. Brédas, and J. Cornil, "Photo induced charge generation and recombination dynamics in model donor/acceptor pairs for organic solar cell applications: a full quantum-chemical treatment," *Journal of the American Chemical Society*, vol. 127, no. 16, pp. 6077–6086, 2005.

[39] R. Shakru, N. J. P. Subhashini, K. kathish, and K. Shivaraj, "Synthesis, characterization and antimicrobial studies on cobalt (II), nickel (II), copper (II) and zinc (II) complexes of N, O, S donor Schiff bases," *Journal of Chemical and Pharmaceutical Research*, vol. 2, pp. 38–46, 2010.

[40] M. A. Halcrow, "Jahn-teller distortions in transition metal compounds, and their importance in functional molecular and inorganic materials," *Chemical Society Reviews*, vol. 42, pp. 1784–1795, 2013.

[41] J. Conradie, M. M. Conradie, K. M. Tawfiq et al., "Jahn-Teller distortion in 2-pyridyl-(1,2,3)-triazole-containing copper (II) compounds," *New Journal of Chemistry*, vol. 42, Article ID 16345, , 2018.

[42] G. A. Zhurko, "Chemcraft-graphical program for visualization of quantum chemistry computations," https://chemcraftprog.com.

[43] M. K. Kesharwani, B. Brauer, and J. M. L. Martin, "Frequency and zero-point vibrational energy scale factors for double-hybrid density functionals (and other selected methods): can anharmonic force fields be avoided?" *The Journal of Physical Chemistry A*, vol. 119, no. 9, pp. 1701–1714, 2015.

[44] R. F. W. Bader, *Atoms in Molecules: A Quantum Theory*, Oxford University Press, Oxford, UK, 1990.

[45] T. Sutradhar and A. Misra, "Theoretical study on the nonlinear optical property of boron nitride nanoclusters functionalized by electron donating and electron accepting groups," *The Journal of Physical Chemistry A*, vol. 125, no. 12, pp. 2436–2445, 2021.

[46] U. Koch and P. L. A. Popelier, "Characterization of C-H-O hydrogen bonds on the basis of the charge density," *Journal of Physical Chemistry*, vol. 99, no. 24, pp. 9747–9754, 1995.

[47] N. Trendafilova, G. Bauer, and T. Mihaylov, "DFT and AIM studies of intramolecular hydrogen bonds in dicoumarols," *Chemical Physics*, vol. 302, no. 1-3, pp. 95–104, 2004.

[48] A. D. Fouegue Tamafo, J. N. Ghogomu, N. K. Nkungli, D. Bikélé Mama, and E. Younang, "Quantum chemical investigation on the antioxidant activity of neutral and anionic forms of juglone: metal chelation and its effect on radical scavenging activity," *Journal of Chemistry*, vol. 2017, Article ID 3281684, 14 pages, 2017.

[49] F. K. Bine, N. K. Nkungli, T. S. Numbonui, and J. Numbonui Ghogomu, "Structural properties and reactive site selectivity of some transition metal complexes of 2, 2′(1E, 1′E)-(ethane-1, 2-diylbis (azan-1-yl-1-ylidene)) bis (phenylmethan-1-yl-1-ylidene) dibenzoic acid: DFT, conceptual DFT, QTAIM, and MEP studies, 2018(1E, 19E)-(ethane-1,2-diylbis(azan-1-yl-1-ylidene))bis(phenylmethan-1-yl-1-ylidene)dibenzoic acid: DFT, conceptual DFT, QTAIM, and MEP studies," *Bioinorganic Chemistry and Applications*, vol. 2018, Article ID 4510648, 11 pages, 2018.

[50] D. Cramer and E. Kraka, "A description of the chemical bond in terms of local properties of electron density and energy," *Croatica Chemica Acta*, vol. 57, pp. 1259–1281, 1984.

[51] R. F. W. Bader and C. F. Matta, "Bonding to titanium," *Inorganic Chemistry*, vol. 40, no. 22, pp. 5603–5611, 2001.

[52] C. Wang, Q.-Y. Wu, X.-H. Kong et al., "Theoretical insights into the selective extraction of americium(III) over europium(III) with dithioamide-based ligands," *Inorganic Chemistry*, vol. 58, no. 15, Article ID 10056, 2019.

[53] A. Srivastava, R. Mishra, S. Kumar, K. Dev, P. Tandon, and R. Maurya, "Molecular structure, spectral investigation (1H NMR, 13C NMR, UV–visible, FT-IR, FT-Raman), NBO, intramolecular hydrogen bonding, chemical reactivity and first hyperpolarizability analysis of formononetin [7-hydroxy-3(4-methoxyphenyl)chromone]: a quantum chemical study," *Journal of Molecular Structure*, vol. 1084, pp. 55–73, 2015.

[54] E. Espinosa, E. Molins, and C. Lecomte, "Hydrogen bond strengths revealed by topological analyses of experimentally observed electron densities," *Chemical Physics Letters*, vol. 285, no. 3-4, pp. 170–173, 1998.

[55] G. A. Jeffrey, *An Introduction to Hydrogen Bonding*, Oxford University Press, Oxford, UK, 1997.

[56] H. Jacobsen, "Localized-orbital locator (LOL) profiles of transition-metal hydride and dihydrogen complexes," *Canadian Journal of Chemistry*, vol. 87, no. 7, pp. 965–973, 2009.

[57] S. Sudha, N. Sundaraganesan, M. Kurt, M. Cinar, and M. Karabacak, "FT-IR and FT-Raman spectra, vibrational assignments, NBO analysis and DFT calculations of 2-amino-4-chlorobenzonitrile," *Journal of Molecular Structure*, vol. 985, no. 2-3, pp. 148–156, 2011.

[58] M. N. Arshad, M. Khalid, G. Shabbir et al., "Donor moieties with D-π-a framing modulated electronic and nonlinear optical properties for non-fullerene-based chromophores," *RSC Advances*, vol. 12, no. 7, pp. 4209–4223, 2022.

[59] N. M. O'boyle, A. L. Tenderholt, and K. M. Langner, "cclib: a library for package-independent computational chemistry algorithms," *Journal of Computational Chemistry*, vol. 29, no. 5, pp. 839–845, 2008.

[60] S. Dheivamalar, L. Sugi, K. Ravichandran, and S. Sriram, "Adsorption of alanine with heteroatom substituted fullerene for solar cell application: a DFT study," *Spectrochimica Acta Part A: Molecular and Biomolecular Spectroscopy*, vol. 202, pp. 333–345, 2018.

[61] R. G. Parr, R. A. Donnelly, M. Levy, and W. E. Palke, "Electronegativity—the density functional viewpoint," *The Journal of Chemical Physics*, vol. 68, no. 8, pp. 3801–3807, 1978.

[62] R. G. Pearson, "Chemical hardness and density functional theory," *Journal of Chemical Sciences*, vol. 117, no. 5, pp. 369–377, 2005.

[63] R. G. Parr, L. V. Szentpaly, and S. Liu, "Electrophilicity index," *Journal of the American Chemical Society*, vol. 121, no. 9, pp. 1922–1924, 1999.

[64] S. Dheivamalar, L. Sugi, and K. Ambigai, "Density functional theory study of exohedral carbon atoms effect on electrophilicity of nicotine: comparative analysis," *Computational Chemistry*, vol. 4, no. 1, pp. 17–31, 2016.

[65] P. K. Chattaraj, S. Giri, and S. Duley, "Update 2 of: electrophilicity index," *Chemical Reviews*, vol. 111, pp. 43–75, 2011.

[66] N. K. Nkungli and J. N. Ghogomu, "Theoretical analysis of the binding of iron (III) protoporphyrin IX to 4 methoxyacetophenone thiosemicarbazone via DFT-D3, MEP, QTAIM, NCI, ELF, and LOL studies," *Journal of Molecular Modeling*, vol. 23, no. 7, p. 200, 2017.

[67] J. D. Huang, K. Yu, X. Huang et al., "Theoretical study of charge-transport and optical properties of organic crystals: 4,5,9,10-pyrenediimides," *IUCrJ*, vol. 6, no. 4, pp. 603–609, 2019.

[68] R. Khatua, S. Debata, and S. Sahu, "Theoretical study on charge transport properties of high mobility n-channel organic semiconductor-hexachloro-hexa-azatrinaphthylene," *Materials Today Proceedings*, vol. 46, no. 14, pp. 6415–6418, 2021.

[69] B. C. Lin, C. P. Cheng, Z.-Q. You, and C.-P. Hsu, "Charge transport properties of tris (8-hydroxyquinolinato) aluminum(III): why it is an electron transporter," *Journal of the American Chemical Society*, vol. 127, no. 1, pp. 66-67, 2005.

[70] L. S. Hung and C. H. Chen, "Recent progress of molecular organic electroluminescent materials and devices," *Materials Science and Engineering: Reports*, vol. 39, no. 5-6, pp. 143–222, 2002.

[71] S. Ten Cate, C. S. S. Sandeep, Y. Liu et al., "Generating free charges by carrier multiplication in quantum dots for highly efficient photovoltaics," *Accounts of Chemical Research*, vol. 48, no. 2, pp. 174–181, 2015.

[72] S. A. Mewes, F. Plasser, A. I. Krylov, and A. Dreuw, "Benchmarking excited-state calculations using exciton properties," *Journal of Chemical Theory and Computation*, vol. 14, no. 2, pp. 710–725, 2018.

[73] T. Lu, "Multiwfn: a multifunctional wavefunction analyzer," 2019, https://sobereva.com/multiwfn.

[74] T. Le Bahers, C. Adamo, and I. Ciofini, "A qualitative index of spatial extent in charge-transfer excitations," *Journal of Chemical Theory and Computation*, vol. 7, no. 8, pp. 2498–2506, 2011.

[75] D. Mester and M. Kállay, "Charge-transfer excitations within density functional theory: how accurate are the most recommended approaches?" *Journal of Chemical Theory and Computation*, vol. 18, no. 3, pp. 1646–1662, 2022.

[76] A. D. Isravel, J. K. Jeyaraj, S. Thangasamy, and W. J. John, "DFT, NBO, HOMO-LUMO, NCI, stability, Fukui function and hole-electron analyses of tolcapone," *Computational and Theoretical Chemistry*, vol. 1202, Article ID 113296, 2021.

[77] A. K. Pal, T. J. Duignan, and J. Autschbach, "Calculation of linear and nonlinear optical properties of azobenzene derivatives with Kohn-Sham and coupled-cluster methods," *Physical Chemistry Chemical Physics*, vol. 20, no. 10, pp. 7303–7316, 2018.

[78] M. J. Frisch, G. W. Trucks, H. B. Schlegel et al., *Gaussian 09, Revision D01*, Gaussian, Wallingford, UK, 2013.